nature portfolio
https://doi.org/10.1038/s41567-021-01427-5

Supplementary information

Evidence for equilibrium exciton condensation in monolayer WTe_2

In the format provided by the
authors and unedited

Supplementary Information:
Evidence for equilibrium exciton condensation in monolayer WTe_2

Bosong Sun[1], Wenjin Zhao[1], Tauno Palomaki[1], Zaiyao Fei[1], Elliott Runburg[1], Paul Malinowski[1], Xiong Huang[2,3], John Cenker[1], Yong-Tao Cui[2], Jiun-Haw Chu[1], Xiaodong Xu[1], S. Samaneh Ataei[4,5], Daniele Varsano[4], Maurizia Palummo[6], Elisa Molinari[4,7], Massimo Rontani[4*], David H. Cobden[1*]

[1]Department of Physics, University of Washington, Seattle, WA 98195, USA

[2]Department of Physics and Astronomy, University of California, Riverside, CA 92521, USA

[3]Department of Materials Science and Engineering, University of California, Riverside, CA 92521, USA

[4]CNR-NANO, Via Campi 213a, 41125 Modena, Italy

[5]Dept of Physics, Shahid Beheshti University, Evin, Tehran 1983969411, Iran

[6]INFN, Dept of Physics, University of Rome Tor Vergata, Via della Ricerca Scientifica 1, 00133 Roma, Italy

[7]Dept of Physics, Informatics and Mathematics, University of Modena and Reggio Emilia, Via Campi 213a, 41125 Modena, Italy

Email: massimo.rontani@nano.cnr.it; cobden@uw.edu

Contents

SI-1 Devices 2

SI-2 Microwave impedance microscopy (MIM) 4

SI-3 Raman spectroscopy measurements 5

SI-4 Notes on anisotropy measurements 6

SI-5 Comparison of chemical potential in two devices. Signs of excitons at 300 K 7

SI-6 Notes on modeling the "V": mobility, overlapping bands, and chemical equilibrium 8

SI-7 Measurements on bilayer WTe_2 9

SI-8 Scaling of excitation energy of lowest direct exciton with inverse number of $\boldsymbol{k}$ points, $\boldsymbol{n_k}$ 10

SI-9 Band dispersion perpendicular to ΓΛ cut of the Brillouin zone 10

SI-10 Crystal growth 10

References 11

SI-1 Devices

We present measurements on five monolayer WTe_2 devices with somewhat different configurations. Devices MW2 and MW3 have top graphite gate and bottom SiO_2/silicon substrate gate. Device MW10 has bottom graphite gate and no top graphite gate, to allow MIM measurements to be performed. Devices MW12 and MW15 have an additional graphene layer with multiple contacts in parallel with the WTe_2 allowing chemical potential measurements. We will also show measurements on bilayer devices BW4 and B2.

The basic fabrication process of a typical device is essentially as follows. First, graphite and hBN crystals are mechanically exfoliated onto a SiO_2/Si substrate. Using the van der Waals (vdW) transfer technique with polycarbonate/polydimethylsiloxane (PC/PDMS) "stamp"[1], the few-layer graphite bottom gate is covered by an hBN flake (bottom hBN). After dissolving the PC polymer in chloroform, the hBN/graphite is annealed at 400 °C for 2h for cleaning. Next, Pt metal contacts (~7 nm) are patterned on the hBN by e-beam lithography and lift-off. Then, WTe_2 crystals are exfoliated in a nitrogen-filled glovebox (O_2 and H_2O concentrations below 0.5 ppm) and monolayers or bilayers are optically identified. A stack of top-gate graphite on hBN, or just hBN, is moved into the glovebox on a stamp, the WTe_2 is picked up under it, and the result is put down on the Pt contacts on hBN. After the PC polymer is dissolved, another step of e-beam lithography, metallization (~7 nm V, ~70 nm Au) and lift-off is used to define wire-bonding pads and connections to the Pt contacts and the top/bottom graphite gates. For devices MW12, MW15 and B2, an extra round of e-beam lithography/metal film deposition/vdW transfer was performed to make the additional graphene layer with its own contacts. Steps in the fabrication of MW15 are shown in Fig. S1. The device capacitance parameters are given in tables T1 and T2. These are purely geometric capacitances, but corrections for finite density of states (quantum capacitance effects) are at the percent level in all cases. This can be deduced from the measurements shown in Fig. S4: the total measured variation of the chemical potential μ in the WTe_2 (~60 meV) is two orders of magnitude smaller than the applied gate voltage (~5 V).

Device label	WTe_2	Top hBN (nm)	Bottom hBN (nm)	C_{tg} (10^{12}e/cm^{2}V)	C_{bg} (10^{12}e/cm^{2}V)
MW2	Monolayer	9.2	17.5	2.4	Si gate
MW3	Monolayer	11.4	14	1.94	Si gate
MW10	Monolayer	N/A	18	N/A	0.92
BW4	Bilayer	10	20.7	2.2	1.07

Table T1. Thickness of the top and bottom hBN and corresponding areal geometric capacitances C_{tg} and C_{bg} between adjacent conductors. The gate-induced electron density is $n_g = C_g V_g / e$, where $C_g = \epsilon_{hBN}\epsilon_0/d_{hBN}$. The effective dielectric constant of hBN is known to depend somewhat on the hBN thickness[2,3]. We used this way for some adjustment to make the critical density n_{ce} for the insulator-metal transition consistent between devices, requiring $\epsilon_{\mathrm{hBN}} = 4$ in devices MW2, MW3, BW4 and $\epsilon_{\mathrm{hBN}} = 3$ in device MW10.

Device	WTe_2	Top hBN (nm)	Middle hBN (nm)	Bottom hBN (nm)	C_{tg} (10^{12}e/cm^{2}V)	C_{mg} (10^{12}e/cm^{2}V)	C_{bg} (10^{12}e/cm^{2}V)
MW12	Monolayer	15	9	N/A	1.1	1.84	N/A
MW15	Monolayer	27	20	11	0.61	0.83	1.51
B2	Bilayer	25	8	N/A	0.89	2.76	N/A

Table T2. Thickness of the top/middle/bottom hBN and corresponding areal geometric capacitances C_{tg}, C_{mg}, C_{bg} for devices including a graphene layer for chemical potential measurements, where $C_g = \epsilon_{hBN}\epsilon_0/d_{hBN}$ and C_{mg} is between the graphene and the WTe_2.

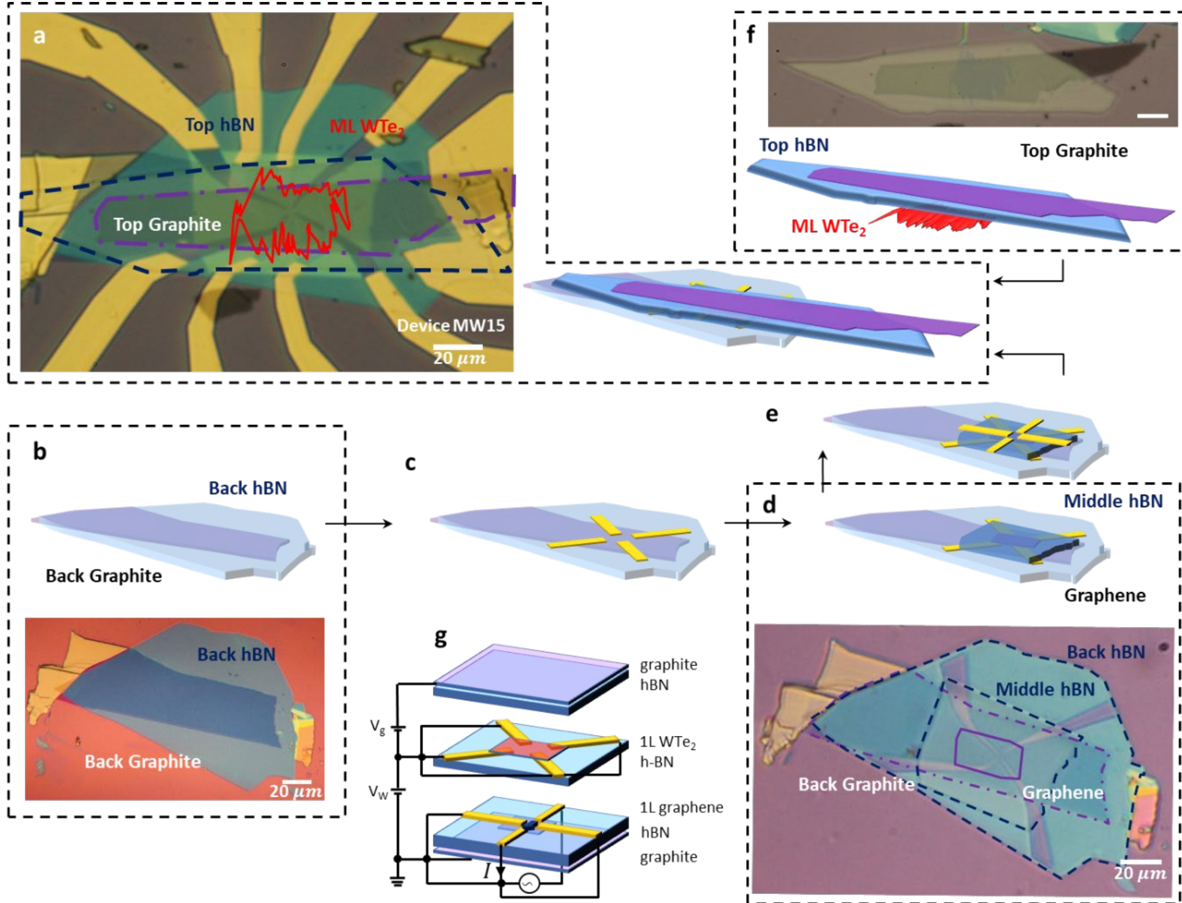

Figure S1. Example of sample fabrication and measurement setup: device MW15. (a) Optical image of device MW15. The monolayer WTe_2 is outlined in red. (b) Bottom hBN and graphite stack preparation. (c) Patterning of metal contacts (7 nm Pt) electrodes for graphene on bottom layer hBN. (d) Transfer of the middle layer hBN and graphene; optical image shows the transfer in progress. (e) Deposition of metal contacts electrodes (7 nm Pt) for monolayer WTe_2 on middle layer hBN. (f) Picking up top graphite/top hBN/monolayer (1L) WTe_2: the optical image shows the pick-up in progress. After transferring the top stack to the prefabricated bottom part, we end up with the device MW15 shown in (a). (g) Setup used with this device to measure μ vs n_e (see Fig. 3a in main text). We use a "current-focusing" geometry employing four electrodes in each layer, as shown. The idea is as follows: when we use the graphene as detector, we apply a bias to one contact with the other three at ground potential, and measure the current to ground in the opposite contact. This current only flows through the center of the cross and so depends mostly on the conductivity of the graphene in that region, which in turn is sensitive to the electric field conditions of only the WTe_2 directly above it. This helps exclude effects of edges, cracks and nonuniformity in the WTe_2 by probing only a small central region of it (see also SI-5 & SI-6).

SI-2 Microwave impedance microscopy (MIM)

Scanning microwave impedance microscopy (MIM) measurements (shown in Fig. 2, main text) were performed in a home-built cryogenic scanning probe microscope[4]. A small microwave signal of $\sim 0.1\ \mu$W at a fixed frequency in the range of 1-10 GHz was delivered to a chemically etched tungsten tip. The reflected signal was analyzed to extract the demodulated output channels, MIM-Im and MIM-Re, which are proportional to the imaginary and real parts of the admittance between the tip and the sample, respectively. The MIM-Im characterizes the sample's capability to screen the oscillating electric field at the tip, while the MIM-Re characterizes the amount of dissipation generated by the screening current. To enhance the MIM signal quality, the tip was excited to oscillate at a frequency of $\sim$32 kHz with an amplitude of $\sim$8 nm. The resulting oscillation amplitudes of MIM-Im and MIM-Re were then extracted using a lock-in amplifier to yield $d(\text{ MIM-Im })/dz$ and $d(\text{ MIM-Re })/dz$, respectively. The $d(\text{ MIM })/dz$ signals are free of fluctuating backgrounds, thus enabling more quantitative analysis. To extract quantitative values of local conductivity from MIM measurements, finite element simulation was performed using COSMOL with known geometrical parameters of the sample. The imaginary and real parts of the tip-sample admittance Y_{ts} were calculated as a function of the sample resistivity at different tip-sample separations, from which dY_{ts}/dz were extracted. MIM signals measured over regions with known electrical properties were used to scale the simulated dY_{ts}/dz to the measured $d(\text{MIM})/dz$. These reference regions include the graphite contact which corresponds to the highly conductive limit, and the nearby hBN substrate with no sample or graphite contact which corresponds to the highly insulating limit.

SI-3 Raman spectroscopy measurements

To perform Raman, a sample was excited at normal incidence by a 632.8 nm excitation laser in backscattering geometry. The laser power was kept below 400 μW to prevent sample degradation. The scattered light was collected and dispersed by a 1200 mm^{-1} groove density grating and detected by a cooled charge-coupled device (CCD) with an integration time of 5 minutes. BragGrate™ notch filters were used to reject Rayleigh scatter down to 5 cm^{-1}. A linear polarizer and half-wave plate (HWP) placed between the notch filter and the sample allow the detection of Raman features that are co-linear with the excitation laser. For angle dependence, the HWP is continuously rotated by 5° continuously until we scan through a full 360°. To save time, we only scanned from 0° to 180° in the temperature dependent measurements and replicated that data for polarizations from 180° to 360°.

Determination of crystal axes. Before assembling a device, the x-axis (W-chain axis) of the monolayer WTe_2 could be guessed from the orientation of nearby larger flakes and tape residue. In the completed devices, polarization-resolved Raman spectroscopy was then used to confirm the alignment. The Raman spectrum of a WTe_2 monolayer is shown in Fig. S2. The peaks near 160 cm^{-1} and 210 cm^{-1} are labelled P10 and P11. In the colinear configuration described above, both are strongest along the y-axis in the monolayer, as seen in Fig. S2b, and bulk samples[5]. We therefore used several bulk WTe_2 flakes with easily identifiable crystal axes to calibrate and verify the alignment between the optical image and incident light polarization.

Search for charge density waves (CDWs). Normally, distinct changes in the Raman spectrum of a layered sample provide a signature of CDW formation due to the associated symmetry change (see, for example, Ref. 6 for the case of 1T-$TiSe_2$). Our detailed study of the temperature dependence of the spectrum of 1L WTe_2 from room temperature down to 15 K (Fig. S2c), well below the appearance of the insulating state, reveals no indication of any such changes. This is consistent with the fact that no clear signs of CDWs have been observed in STM (see, e.g. Refs. 7–9).

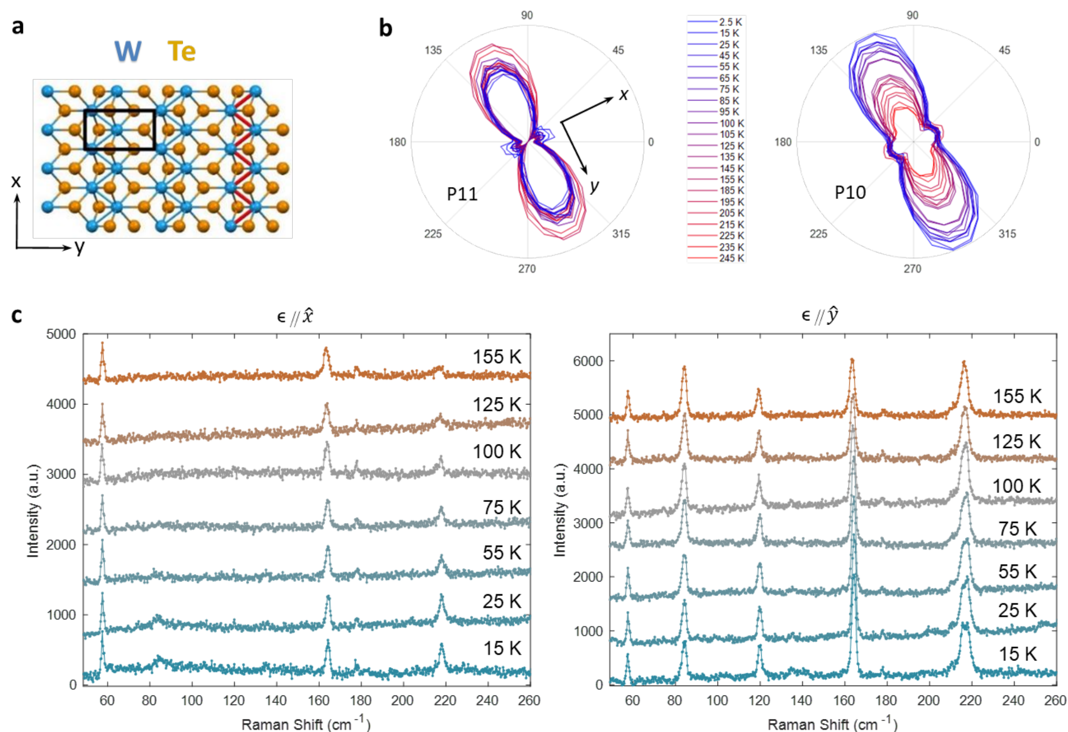

Figure S2. Raman Spectroscopy. (a) Structure of 1L WTe_2 seen from above; the x-axis is taken along the W chains. (b) Anisotropy of peaks P11 (210 cm^{-1}) and P10 (160 cm^{-1}) for colinear polarization at a series of temperature. (c) Raman intensity for polarization parallel to x-axis and y-axis at a series of temperatures, showing no distinct changes across the entire temperature range that could indicate CDW formation.

SI-4 Notes on anisotropy measurements

We here briefly provide more discussion of the measurements shown in Fig. 2c of the main text. Since the edges of monolayer WTe_2 conduct, and there are often cracks present which effectively produce internal edges, we use the “empty cross” contact pattern sketched in Fig. S3a to minimize the effect of such cracks and edges. In devices with no top gate, such as MW10, MIM can be used to identify empty crosses where there are no cracks nearby. We then apply a bias to one contact and collect the current to ground from the opposite contact with the other two contacts directly grounded. Most of the collected current then passes only through the center region of the cross and flows roughly parallel to the line joining the contacts, hence probing the conductivity in this direction. We confirmed this by simulating the current flow for a uniform conducting sheet with contacts in this shape using finite-element analysis algorithms, corresponding to solving an anisotropic Laplace equation with mixed boundary conditions. Fig. S3b shows the region probed by 95% of current flowing in this particular geometry, here taking the conductivity to be isotropic.

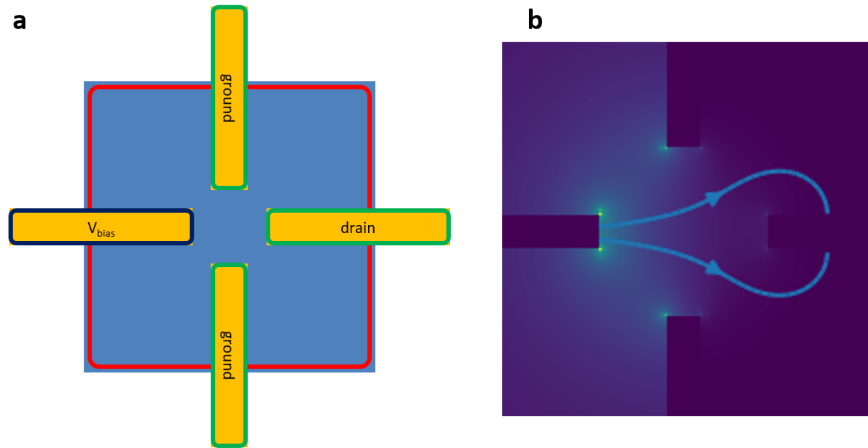

Figure S3. (a) Contact and boundary geometry for a current distribution simulation. Red line: boundary of 1L WTe_2 (assumed to be a uniform 2D conductor), where normal current density vanishes (and we neglect edge conduction). Blue line: equipotential at $V = V_{bias}$. Green line: equipotential at $V = 0$. (b) Current streamlines enclosing 95% of the current flowing from the left to the right contact.

SI-5 Comparison of chemical potential in two devices. Signs of excitons at 300 K

The measurements on device MW12, presented in Fig. 3 of the main text, are compared with similar measurements on similar device MW15 in Fig. S4. Their behavior is consistent, except that in MW15 the step in μ is not as steep and the "V" in the conductance is more rounded. It is very likely that this is a result of greater sample inhomogeneity in MW15. The measurements on MW15, however, extend to 300 K and show that some residual step is present in the chemical potential at the neutral point even at 300 K, even though the step height is much less than kT (green bar), suggesting that excitonic effects are relevant up to room temperature.

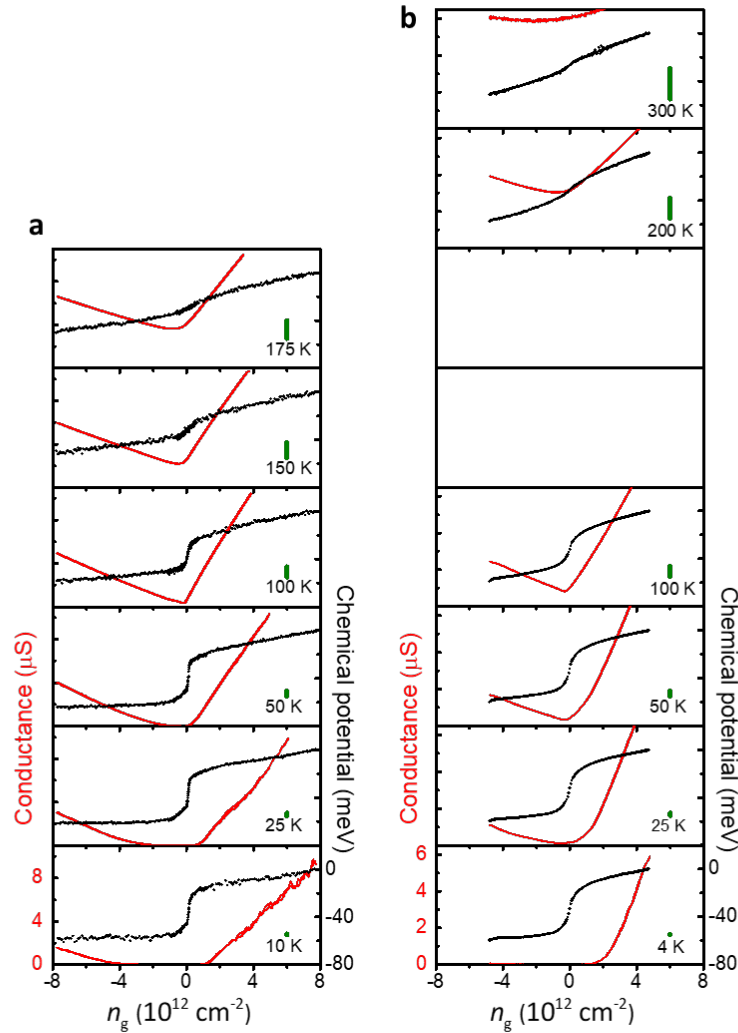

Figure S4. (a) Measurements of chemical potential μ (black) and conductance G_p (red) vs. gate doping n_g on 1L WTe_2 device MW12, reproduced from Fig 3(b) in the main text. (b) Comparable measurements on device MW15. The zero of μ is chosen arbitrarily at each temperature.

SI-6 Notes on modeling the "V": mobility, overlapping bands, and chemical equilibrium

To aid the following discussion, Fig. 4a-c of the main text is reproduced as Fig. S5a-c.

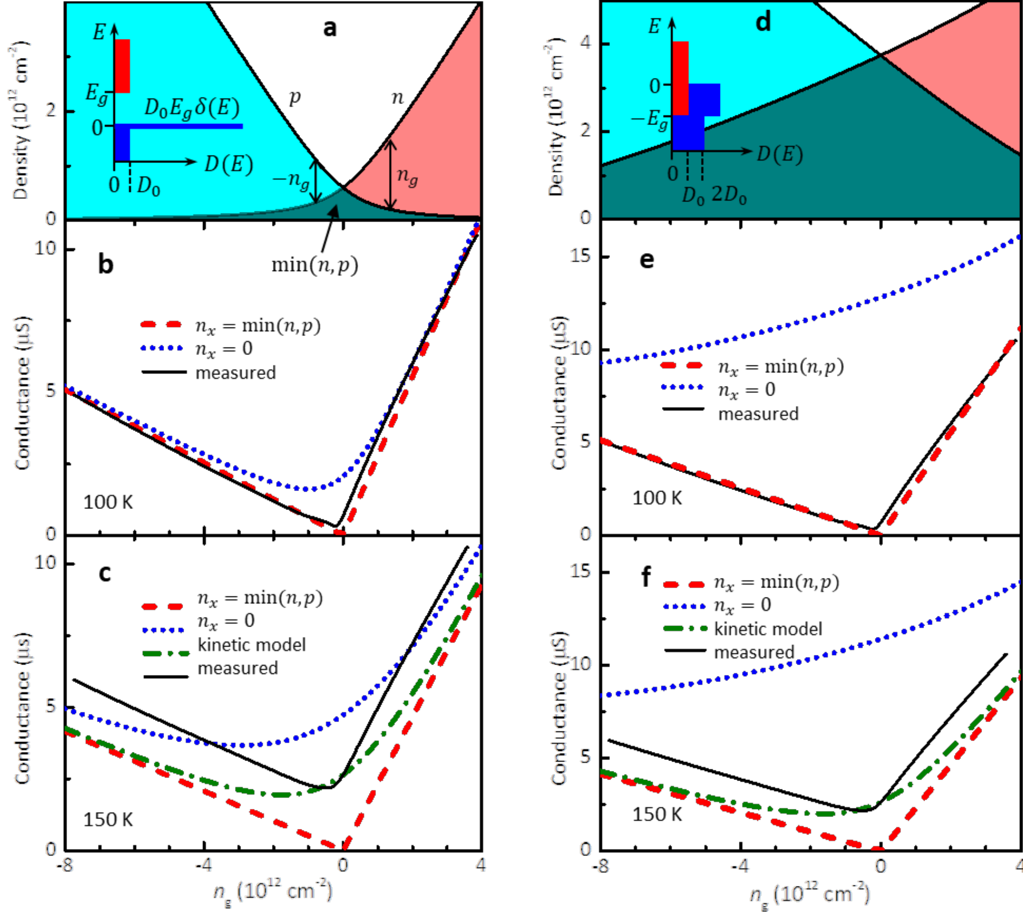

Figure S5. (a-c) Same as Fig. 4 in the main text, using the gapped density of states shown in Fig. 3 and in the inset to (a). (d-f) Corresponding graphs using overlapped bands, as shown in the inset to (d).

Mobility. In our argument that electron-hole pairing helps explain the sharp "V", we compared the conductance data at 100 K (black trace in Fig. S5b) with the simple model where all minority carriers are bound, $n_x = \min(n,p)$ (red dashed trace). Then, (neglecting contact resistance R_c because G_p is small near zero doping), $G_p = \beta^{-1}\sigma = \beta^{-1}\mu_e e n_g$ for $n_g > 0$ and $G_p = -\beta^{-1}\mu_h e n_g$ for $n_g < 0$. Since the geometric factor β is unknown, we cannot determine the absolute mobilies accurately. In addition, we know the conductivity is anisotropic but we do not know the orientation of the current relative to the axis in this device. This is unimportant, however, as our objective is simply understanding the linear "V" shape. We therefore treat $\beta^{-1}e\mu_e$ and $\beta^{-1}e\mu_h$ as parameters to achieve the best fit at each temperature; their values are unimportant but for completeness at 100 K they are $\beta^{-1}e\mu_e = 2.72 \times 10^{-12}$ μS cm^2 and $\beta^{-1}e\mu_h = 0.64 \times 10^{-12}$ μS cm^2 and at 150 K they are $\beta^{-1}e\mu_e = 2.33 \times 10^{-12}$ μS cm^2 and $\beta^{-1}e\mu_h = 0.52 \times 10^{-12}$ μS cm^2.

Effect of overlapping bands. The blue dotted lines in Figs. S5b and c are plots of $\sigma = \mu_e n + \mu_h p$, where $n = \int_{-\infty}^{+\infty} D_c(E) f(E) dE$ and $p = \int_{-\infty}^{+\infty} D_v(E)(1 - f(E)) dE$ calculated using the gapped single-particle spectrum shown in the left inset taking $E_g = +43$ meV. To illustrate the effect of modifying $D(E)$, in Figs. S5d-f we show the result of doing the same calculations but with the c and v bands overlapping, i.e., with a negative gap $E_g = -40$ meV, as shown in the right inset. Here we have no δ-function at the v band edge and set $D_v/D_c = 1/2$ simply because $n_{ce}/n_{cp} \sim 2$. Although n and p are

now much larger (Fig. S5d), and without excitons the model conductance varies smoothly with n_g (Fig. S5e) at odds with the data, if we assume again that $n_x = \min(n, p)$ then naturally we get the same "V" shape, matching the data at 100 K (red dashed), as when using the gapped spectrum.

Chemical equilibrium considerations. As mentioned in the main text, one may also ask whether the observed behavior above 100 K could be explained by a variation of the exciton density with n_g. To make it clear that this is not feasible, we consider a variation based on simple chemical equilibrium between the excitons and free particles, i.e.,

$$n_x = K(n - n_x)(p - n_x)\,,$$

where K is an equilibrium constant[10]. For simplicity we assume K is independent of n_g for a given temperature. Solving for n_x gives

$$n_x = \frac{1}{2}\left[n + p + \frac{1}{K} - \sqrt{\left(n + p + \frac{1}{K}\right)^2 - 4np}\right].$$

The green dash-dotted lines in Figs. S5c and S5f are plots of $\sigma = \mu_e(n - n_x) + \mu_h(p - n_x)$ using the above expression for n_x with K chosen to match the measured conductance at $n_g = 0$ and using the same $\beta^{-1}\mu_{e,h}$ values as before. The agreement with the data remains poor, irrespective of the single-particle spectrum. The chemical equilibrium condition does not prevent thermal smearing, and also it causes to n_x to approach $\min(n, p)$ as $|n_g|$ increases, making the calculated conductance too small at high gate voltages.

SI-7 Measurements on bilayer WTe_2

Conductance and chemical potential measurements on bilayer WTe_2 (Fig. S6) show striking similarities to those on monolayers. The conductance of bilayer is more straightforward to measure because it lacks edge conduction; on the other hand, the ferroelectric switching complicates the chemical potential measurements[11]. A sharp "V" develops in conductance vs gate voltage (Fig. S6a) at the neutral point at around 20 K, while there is a step in the chemical potential (Fig. S6b) of size ~10 meV that is fully developed below 20 K. This suggests that similar excitonic physics is at play in the bilayer but at a ~5 times smaller energy scale than that in the monolayer. Trilayer WTe_2 is metallic.

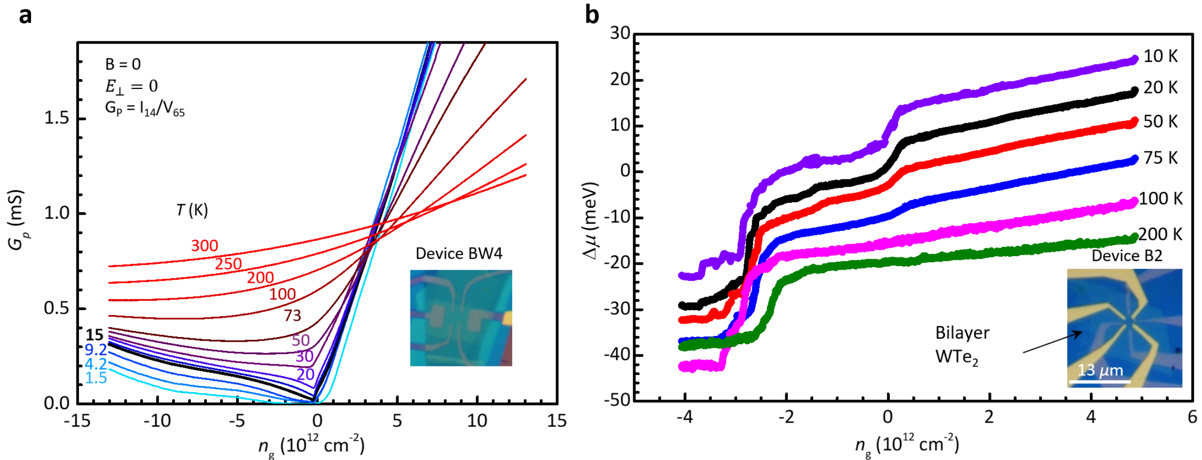

Figure S6 (a) Conductance characteristics of 2L WTe_2 device BW4 (for zero displacement field). Here the inverse 4-terminal resistance is plotted. (b) Chemical potential. Ferroelectric switching in the bilayer limits the range of the chemical potential measurement: these measurements are all performed sweeping n_g downwards in a single polarization state.

SI-8 Scaling of excitation energy of lowest direct exciton with inverse number of $\boldsymbol{k}$ points, $\boldsymbol{n_k}$

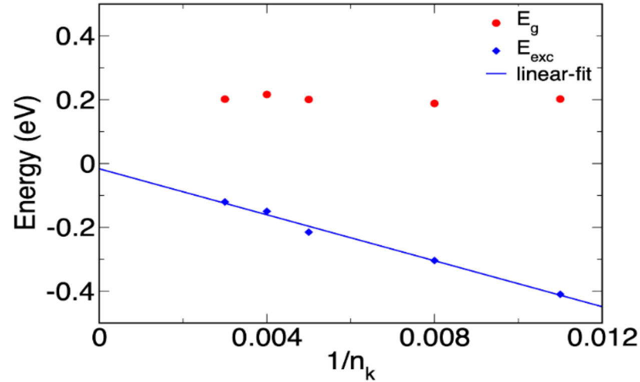

Figure S7. Plot of the direct band gap (E_g, red dots; not to be confused with the absolute, indirect band gap) and excitation energy of the lowest exciton with momentum $\boldsymbol{q} = 0$ (blue diamonds, E_{exc}), versus inverse number of irreducible $\boldsymbol{k}$ points, $1/n_k$. The solid line is the linear regression of the excitation energy on $1/n_k$. The difference between the energy extrapolated for $1/n_k = 0$ and the value obtained for the largest implemented sampling is 100 meV, which is the uncertainty induced by the numerical discretization of $\boldsymbol{k}$-space, shown by the error bars in Fig. 5b (main text).

SI-9 Band dispersion perpendicular to ΓΛ cut of the Brillouin zone

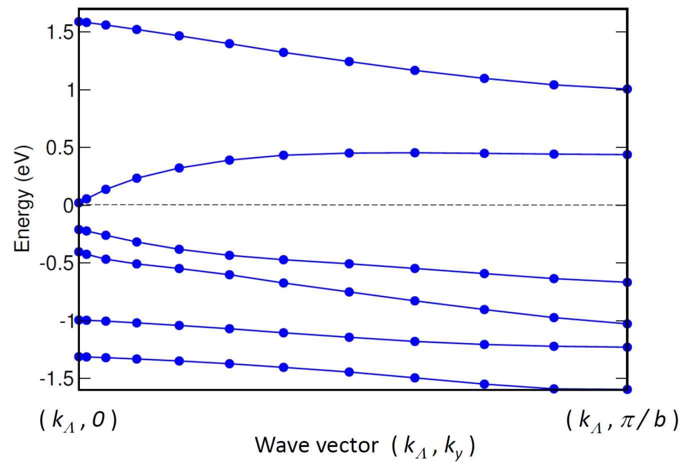

Figure S8. Calculated bands from first principles (DFT-PBE0 level, see Methods) along the cut of the Brillouin zone parallel to ΓY and intersecting the Λ point. The plot is a companion to Fig. 5a in the main text which is along the ΓX cut.

SI-10 Crystal growth

WTe_2 single crystals were grown out of a Te-rich self-flux with the following procedure[12]. Elemental W power and Te shot were loaded into alumina crucibles in the molar ratio 1:50 with a total charge of 3.5 g. The crucibles were loaded into quartz tubes and sealed under an evacuated argon atmosphere. The tubes were then placed in a box furnace and heated to 1000 °C over 12 hours, held at 1000 °C for 12 hours, cooled for 460 °C over 100 hours, and finally decanted at 460 °C via centrifuge. This procedure resulted in large, high quality single crystals of WTe_2 with ribbon-like morphology and typical dimensions 5 mm × 0.3 mm × 0.01 mm.

References

1. Zomer, P. J., Guimarães, M. H. D., Brant, J. C., Tombros, N. & van Wees, B. J. Fast pick up technique for high quality heterostructures of bilayer graphene and hexagonal boron nitride. *Appl. Phys. Lett.* **105**, 013101 (2014).
2. Zhao, W. *et al.* Magnetic proximity and nonreciprocal current switching in a monolayer WTe_2 helical edge. *Nature Materials* **19**, 503–507 (2020).
3. Xu, S.-Y. *et al.* Electrically switchable Berry curvature dipole in the monolayer topological insulator WTe_2. *Nature Physics* **14**, 900–906 (2018).
4. Shi, Y. *et al.* Imaging quantum spin Hall edges in monolayer WTe_2. *Science Advances* **5**, eaat8799 (2019).
5. Kim, M. *et al.* Determination of the thickness and orientation of few-layer tungsten ditelluride using polarized Raman spectroscopy. *2D Mater.* **3**, 034004 (2016).
6. Duong, D. L. *et al.* Raman Characterization of the Charge Density Wave Phase of 1T-$TiSe_2$: From Bulk to Atomically Thin Layers. *ACS Nano* **11**, 1034–1040 (2017).
7. Tang, S. *et al.* Quantum spin Hall state in monolayer 1T'-WTe_2. *Nature Physics* **13**, 683–687 (2017).
8. Song, Y.-H. *et al.* Observation of Coulomb gap in the quantum spin Hall candidate single-layer 1T '-WTe_2. *Nature Communications* **9**, 4071 (2018).
9. Lupke, F. *et al.* Proximity-induced superconducting gap in the quantum spin Hall edge state of monolayer WTe_2. *Nature Physics* **16**, 526–530 (2020).
10. Siviniant, J., Scalbert, D., Kavokin, A. V., Coquillat, D. & Lascaray, J.-P. Chemical equilibrium between excitons, electrons, and negatively charged excitons in semiconductor quantum wells. *Phys. Rev. B* **59**, 1602–1604 (1999).
11. Fei, Z. *et al.* Ferroelectric switching of a two-dimensional metal. *Nature* **560**, 336–339 (2018).
12. Wu, Y. *et al.* Temperature-Induced Lifshitz Transition in WTe_2. *Phys. Rev. Lett.* **115**, 166602 (2015).